

Topological surface states of MnBi_2Te_4 at finite temperatures and at domain walls

Kevin F. Garrity,* Sugata Chowdhury, and Francesca M. Tavazza

Material Measurement Laboratory, National Institute of Standards and Technology, Gaithersburg MD, 20899

(Dated: May 13, 2022)

MnBi_2Te_4 has recently been the subject of intensive study, due to the prediction of axion insulator, Weyl semimetal, and quantum anomalous Hall insulator phases, depending on the structure and magnetic ordering. Experimental results have confirmed some aspects of this picture, but several experiments have seen zero-gap surface states at low temperature, in conflict with expectations. In this work, we develop a first-principles-based tight-binding model that allows for arbitrary control of the local spin direction and spin-orbit coupling, enabling us to accurately treat large unit-cells. Using this model, we examine the behavior of the topological surface state as a function of temperature, finding a gap closure only above the Néel temperature. In addition, we examine the effect of magnetic domains on the electronic structure, and we find that the domain wall zero-gap states extend over many unit-cells. These domain wall states can appear similar to the high temperature topological surface state when many domain sizes are averaged, potentially reconciling theoretical results with experiments.

Since the pioneering work of Haldane¹, there has been great interest in the topological properties of materials systems, with many exciting developments in the past dozen years^{2–4}. However, much of the progress on topological systems has been focused on topological classes with time-reversal symmetry (TRS), and topological materials with broken TRS, *i.e.* magnetic materials, remain challenging to design and study. The zero-field quantum anomalous Hall effect in particular has only been realized in magnetically-doped topological insulators, with sub-Kelvin temperatures necessary to observe robust quantization, limiting possible applications of this effect^{5–8}.

MnBi_2Te_4 and MnBi_2Se_4 have recently been the subject of intensive study^{9–23}, due to theoretical predictions^{24–29} that they are antiferromagnetic (AFM) topological insulators (TI), a type of axion insulator, in bulk^{30–33}. In addition, they can display Weyl semimetal phases under strain and/or external magnetic field. In two-dimensional geometries, they are predicted to be Chern insulators for systems with an odd number of layers. This materials class offers the possibility of observing broken-TRS topological effects in single-crystal materials with reasonably high magnetic transition temperatures ($T_N \approx 24$ K²⁶) and larger band gaps, which should improve the robustness of the topological effects. However, there has been some disagreement between experiments and theoretical expectations, and in some cases between different experiments, on fundamental properties of this material. Under external magnetic field sufficient to drive a transition from the layered AFM ground state to a fully spin-polarized ferromagnetic (FM) state, the quantum anomalous Hall effect has been observed, as expected, but the anomalous Hall conductivity (AHC) of odd-layer systems is not observed to be quantized at zero field^{11,12}. In addition, several experiments have observed surface state features even below the Néel temperature^{14–18,26,34}, which are expected to be gapped by the broken TRS on the surface, while other experiments have seen inconsistent or conflicting results^{6,13,14,19,35} (see discussion in Ref. 18).

To address these discrepancies, in this work, we develop a first principles-based model of the magnetic degrees of freedom and electronic structure of MnBi_2Te_4 that can be applied to large unit cells. Using this model, we first briefly consider the iso-symmetric topological transition that occurs as a function of spin-orbit coupling (SOC) strength. Next, we study the temperature-driven topological phase transition that accompanies the Néel transition, observing how the bulk and surface band structures change in response to changes in the spin ordering. We find that consistent with expectations, the system has a bulk band gap both above and below the transition temperature, but only has a surface state above T_N when TRS is restored. Finally, we study domain walls in low temperature MnBi_2Te_4 , which can be understood as a type of topological transition that occurs as a function of spatial location. We find spin-polarized metallic edge states localized on the surface at the domain walls, but that extend over many unit-cells along the surface perpendicular to the domain wall. These surface features can appear similar to the topological surface states we observe in the disordered spin configurations, which may help reconcile some of the unexpected experimental observations with theory.

We perform first principles density functional theory (DFT) calculations^{36,37} with the Quantum Espresso code³⁸ using the PBEsol³⁹ functional. We use a DFT+U correction with $U=3$ eV on the Mn- d states^{40–42}. We use norm-conserving ONCV pseudopotentials with SOC^{43–45}. We use Wannier90^{46–49} to generate first principles tight-binding Hamiltonians, and we calculate topological invariants with both WannierTools⁵⁰ and our own code. Our initial Wannier projection consists of Bi/Te- p orbitals and Mn- d orbitals, which describes all the bands near the Fermi level. For our model of magnetic interactions, we fit a spin-spin Heisenberg model plus onsite anisotropy with fixed crystal structure⁵¹. We generate magnetic configurations in the equivalent of a $2 \times 2 \times 2$ and $3 \times 3 \times 3$ unit cells, using the method of Lloyd-Williams *et al.* to generate smaller non-diagonal cells⁵².

In order to calculate the electronic structure of the large unit-cells that are necessary to treat structures with disordered spins or domain walls, we develop a tight-binding model, based on Wannier Hamiltonians, that allows us to calculate the electronic structure for arbitrary orientations of the Mn spins, as well as variable SOC. The model is similar in spirit to the model in Ref. 53, which treats chemical disorder in topological insulators. The basis of our model is three separate DFT plus Wannier calculations. First, we perform a calculation with TRS and without SOC, getting the Hamiltonian H^{TRS} . Second, we perform a calculation with TRS and SOC, getting H_{SOC}^{TRS} . By subtracting these two Hamiltonians, we can isolate the SOC contribution, $H_{SOC} = H_{SOC}^{TRS} - H^{TRS}$. Finally, we perform a FM calculation without SOC, which is separated into independent spin up (H^{up}) and spin down (H^{dn}) terms.

We then assemble the total model for a single unit-cell, H_{tot} :

$$H_{avg} = \frac{1}{2}(H^{up} + H^{dn}) \quad (1)$$

$$H_{diff} = \frac{1}{2}(H^{up} - H^{dn}) \quad (2)$$

$$H_{tot} = H_{avg}\sigma_0 + H_{diff}(\mathbf{m} \cdot \boldsymbol{\sigma}) + H_{SOC}, \quad (3)$$

where the vector \mathbf{m} is the normalized magnetization direction, σ_0 is the identity matrix, and $\boldsymbol{\sigma}$ are the three Pauli matrices. To generate tight-binding Hamiltonians for supercells with different magnetic orderings (\mathbf{m} 's) in each cell, we keep the onsite terms as above and average the inter-cell matrix elements. To construct surfaces, we create supercells of the desired thickness, but then set to zero any hoppings that would go across the surface. This approximation is reasonable for MnBi_2Te_4 because of the layered crystal structure, and direct surface calculations show that the surface relaxation energy of MnBi_2Te_4 is only 5 meV per surface unit cell. We can also artificially adjust the magnitude of the SOC by multiplying the final term in the model by a number between zero and one.

In order to verify the accuracy of this model, we compare the model band structure to equivalent calculations done directly with DFT-derived Wannier Hamiltonians for several spin configurations. In Fig. 1a and b, we show the DFT and model band structures for the ground state AFM phase with spins in the $\pm z$ -direction. Comparing the two figures, we find excellent agreement, with all major features of the band structure reproduced by the model. We emphasize that the model is built using only FM spin configurations and only non-magnetic SOC calculations, so its success describing an AFM calculation with SOC is encouraging. We show several more bulk band structure comparisons with various spin orderings in Fig. S1 of the supplementary materials (SM). In Fig. S2, we directly compare a three-layer thick surface DFT calculation with our model. In both cases we find excellent agreement. In order to interpret the band structures of systems with large unit cells and magnetic disorder, we use band unfolding to produce effective primitive

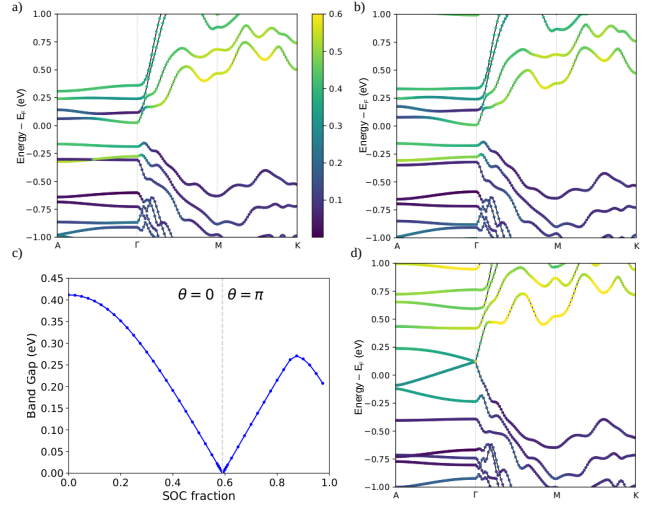


FIG. 1. a) Band structure of AFM phase with spins in z -direction calculated using DFT. b) Same, but calculated with model. The colors show projections onto Bi Wannier functions. c) Band gap in eV as a function of SOC fraction. d) Model band structure at SOC=0.59, the critical value.

cell spectral functions^{53–56}.

Using our tight-binding model, we can now study changes in the electronic structure during several types of topological phase transitions. As a warm-up, we first consider the iso-symmetric topological transition that occurs when artificially varying the strength of the SOC. In Fig. 1c, we show the band gap of the ground state AFM phase as a function of the strength of SOC. The non-trivial AFM topological state of MnBi_2Te_4 is driven by SOC-induced band inversion, therefore, at zero SOC, MnBi_2Te_4 is a trivial AFM insulator. As the fraction of SOC is increased, the bulk band gap closes, and at the critical value of the SOC, 0.59, the the band structure becomes inverted. Above this value, our model is in a topologically non-trivial AFM insulating phase, which is also an axion insulator. This transition is an example of an iso-symmetric transition between a topologically non-trivial and trivial state, as a function of an external tuning parameter, which requires a bulk gap closure. In practice, directly controlling the SOC experimentally is not possible, but this transition might be similar to a topological transition that occurs as a function of doping.

Next, we consider the topological phase transition that occurs as a function of temperature. Above the Néel temperature, the spins in MnBi_2Te_4 become disordered, restoring TRS on average. Similar to previous works on this material class^{24,26}, we use a classical Heisenberg spin model, plus an onsite anisotropy term, to calculate the energy of various spin configurations, and we generate configurations at a given temperature using Metropolis Monte Carlo^{57,58}. For more details, see the supplementary materials section II. We find that our model has a transition temperature of 40 K, which is in reasonable agreement with experiment, considering that quantum

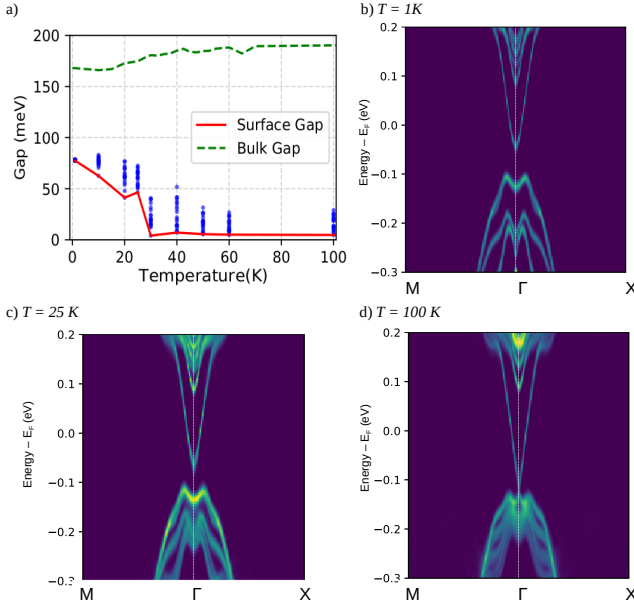


FIG. 2. a) Band gap (meV) versus temperature. Solid red line: minimum surface gap. Dashed green line: mean bulk gap. Blue points: individual surface calculations. b-d) Unfolded average surface band structure at 1 K, 25 K and 100 K, respectively.

fluctuations lower transition temperatures. As expected for a layered structure, we find that within-layer spin-spin correlations are much larger than inter-layer correlations, and remain small but non-zero above the transition temperature.

Using our magnetic model, we can generate spin configurations at a given temperature, and then study the average electronic structure using our tight-binding model. We first perform this analysis in a periodic $3 \times 3 \times 6$ unit cell without a surface. We confirm that the bulk gap does not close during near T_N , and in fact opens slightly, as shown by the dashed line in Fig. 2a (see also supplementary materials Fig. S5-S6). Unlike the iso-symmetric SOC-driven transition studied above, here, the order-to-disorder spin transition restores TRS at high temperatures. Because of the symmetry change, the relevant topological invariants are different above and below T_N , and no bulk gap closure is required despite the topological transition.

Next, we monitor the same transition, but in $3 \times 3 \times 5$ unit-cell, with surfaces perpendicular to the z -direction. In this odd-layered case, we find that MnBi_2Te_4 is a Chern insulator at zero temperature, consistent with previous work^{24–26}. In Fig. 2a, the blue points are the gaps of individual spin configurations, and the solid red line shows the minimum gap at each temperature. We find that above T_N , the minimum surface gap closes. Individual spin configurations can have small gaps of ≈ 25 meV even above T_N , which we attribute to spin fluctuations breaking TRS. We expect that unit-cells with larger areas than we can easily calculate would have smaller mini-

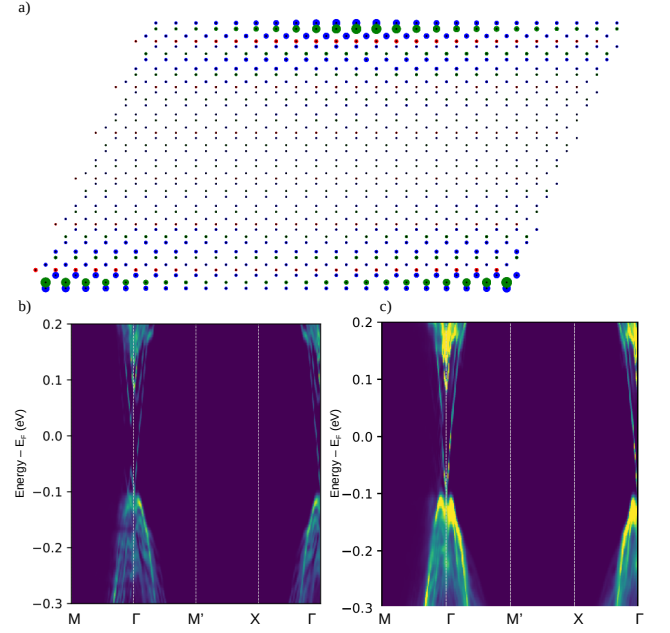


FIG. 3. a) Real-space representation of $|\psi|^2$ localized at domain wall in $24 \times 1 \times 5$ cell. Larger circles have more weight. Blue circles are Te, green are Bi, and red are Mn. b) Unfolded band structure in $20 \times 1 \times 5$ unit cell with 10 unit cell domains. c) Average unfolded band structure (see text).

mum gap fluctuations above T_N , but that a spatially local measurement of the gap would continue to fluctuate.

In Figs. 2b-d, we show the unfolded surface band structure, averaged over 20 spin configurations, at $T = 1$ K, 25 K, and 100 K, respectively. At low temperature, when the spins are almost perfectly aligned, we find sharply defined bands and a clear band gap. However, as the temperature is raised to 25 K, which is slightly below the Néel temperature in our model, the bands become more diffuse, and the spin-polarized bands begin to show the influence of disorder. In addition, the gap at Γ begins to close. Finally, at 100 K, we find a closed gap, with a clear Dirac cone surface feature, which shows that the system is in a non-trivial TRS-invariant ($Z_2 = 1$) topological insulating state. This average topological state emerges despite the fact that the individual band structures that go into the average break TRS.

The above discussion of temperature-driven topological states provides a clear explanation of the surface features observed experimentally above T_N ; however, the states observed at low temperature remain unexplained. One possible explanation is that the low temperature surface spin configuration does not match the theoretical predictions. However, in this section, we consider the alternate explanation that there is a significant density of domains in the AFM phase at low temperature, possibly pinned by sample dependent defects. In the bulk of an AFM topological insulator, the topological index on either side of a domain boundary is the same, as the spin configurations are related by a translation by one

layer in the z -direction. Therefore, a gap closure at the domain wall is not required. Equivalently, the axion angle of both domains equals $\pi \pm 2\pi^{30,33}$. However, in the presence of a surface, this translation is no longer possible. Each surface of an AFM TI contributes $\pm \frac{e^2}{2h}$ to the total AHC, with the sign determined by the direction of the spins in the top layer³⁰. Therefore, there are two distinct topological phases at the surface of an AFM TI, and a domain wall between these surfaces must have a 1D conducting channel that contributes a total of $\pm \frac{e^2}{h}$ to the AHC. In this work, we consider sharp Ising-like domain walls, where the spins suddenly change from $+z$ to $-z$, or vice versa, at the boundary. Of course, more complicated configurations where the spins rotate gradually (Bloch-like) are also possible; however, we will find that even sharp interfaces result in extended conducting states. Furthermore, we note that similar considerations apply to step edges.

Using our model, we first study domains in a $24 \times 1 \times 5$ unit cell, with surfaces in the z direction, with two domains 12 unit cells wide, and therefore two domain walls. As expected, we find a gap closure at $k = \Gamma$, with four degenerate states. These states correspond to the states localized at the two domain walls on each surface, although at the degeneracy point they are all mixed together. To make the plotting clearer, we move slightly away from Γ , and consider two empty degenerate states at $k_x = 0.05 \frac{2\pi}{a}$. In Fig. 3a, we plot $|\psi|^2$ for that pair of states, using larger circles to represent larger magnitudes of the eigenvector. We find that as expected, the pair of eigenvectors are surface states localized at the domain walls at $x = 0$ and $x = 0.5$ on the bottom and top surfaces. Even though we fix the spins to reverse direction abruptly at the domain wall, we see that the electronic states decay rather slowly perpendicular to the domain wall, extending ≈ 10 unit cells around the wall.

In Fig. 3b, we consider the unfolded band structure for a single example of a pair of domains, in a $20 \times 1 \times 5$ unit cell. We see that there is a gap closure at Γ , and that the bandstructure looks somewhat similar to the 2D topological surface state for disordered spins (see Fig. 2d), even though the metallic edge channel is 1D. However,

because we are only considering a single pair perfectly ordered and periodic domains, the unfolded topological surface band has a variety of artifacts related to wavevectors of the superlattice. In an experimental situation, we expect that there will instead be domains of varying sizes. Therefore, in Fig. 3c, we average the unfolded surface band structures of dozens of similar domains, with thicknesses of 4 to 10 unit cells, in supercells of 8 to 20 unit cells. We see that we recover an average band structure that looks quite similar to the 2D topological surface state with disordered spins shown in Fig. 2d, even though every spin is perfectly aligned along the $\pm z$ direction and the domain walls are sharp and aligned. We expect that if we go even further and include configurations with partially disordered spins and domain walls in varying directions, the result will be band structures that closely resemble the Dirac cone features we see at high temperatures.

In conclusion, we generated a model to study the electronic structure of large unit cells of the AFM topological insulator MnBi_2Te_4 with arbitrary spin configurations, which we have used to study three types of topological phase transitions. First, we considered an artificial transition driven by adjusting the magnitude of the SOC, which proceeds via a bulk gap closure. Next, we considered a topological transition driven by a temperature dependent magnetic ordering. We find that as TRS is restored on average above T_N , MnBi_2Te_4 goes from an AFM topological insulator with a surface gap to a TRS-invariant Z_2 topological insulator with an associated Dirac cone surface state, but with minimal change in the bulk gap. Finally, we consider the electronic surface states associated with AFM domain walls, which are 1D topological states. We find that these states are strongly localized at the surface, but extend many unit cells perpendicular to the domain walls, and that many 1D domain walls can together resemble a Dirac cone-like topological surface state on average. This work suggests that further experiments to quantify the domain structure of AFM MnBi_2Te_4 and to directly observe the localized states expected at domain walls may clarify aspects of the topology and transport in this material.

* kevin.garrity@nist.gov

¹ F. D. M. Haldane, Phys. Rev. Lett. **61**, 2015 (1988).

² M. Z. Hasan and C. L. Kane, Rev. Mod. Phys. **82**, 3045 (2010).

³ X.-L. Qi and S.-C. Zhang, Rev. Mod. Phys. **1057**, 1057 (2011).

⁴ Y. Tokura, K. Yasuda, and A. Tsukazaki, Nature Reviews Physics **1**, 126 (2019).

⁵ Y. Chen, J.-H. Chu, J. Analytis, Z. Liu, K. Igarashi, H.-H. Kuo, X. Qi, S.-K. Mo, R. Moore, D. Lu, *et al.*, Science **329**, 659 (2010).

⁶ C.-Z. Chang, J. Zhang, X. Feng, J. Shen, Z. Zhang, M. Guo, K. Li, Y. Ou, P. Wei, L.-L. Wang, *et al.*, Science **340**, 167

(2013).

⁷ C.-Z. Chang, W. Zhao, D. Y. Kim, H. Zhang, B. A. Assaf, D. Heiman, S.-C. Zhang, C. Liu, M. H. Chan, and J. S. Moodera, Nature materials **14**, 473 (2015).

⁸ I. Lee, C. K. Kim, J. Lee, S. J. Billinge, R. Zhong, J. A. Schneeloch, T. Liu, T. Valla, J. M. Tranquada, G. Gu, *et al.*, Proceedings of the National Academy of Sciences **112**, 1316 (2015).

⁹ D. S. Lee, T.-H. Kim, C.-H. Park, C.-Y. Chung, Y. S. Lim, W.-S. Seo, and H.-H. Park, CrystEngComm **15**, 5532 (2013).

¹⁰ J. A. Hagmann, X. Li, S. Chowdhury, S.-N. Dong, S. Rouvimov, S. J. Pookpanratana, K. M. Yu, T. A. Orlova, T. B.

- Bolin, C. U. Segre, *et al.*, New Journal of Physics **19**, 085002 (2017).
- ¹¹ Y. Deng, Y. Yu, M. Z. Shi, J. Wang, X. H. Chen, and Y. Zhang, “Magnetic-field-induced quantized anomalous hall effect in intrinsic magnetic topological insulator mnbi_2te_4 ,” (2019), arXiv:1904.11468 [cond-mat.mtrl-sci].
 - ¹² C. Liu, Y. Wang, H. Li, Y. Wu, Y. Li, J. Li, K. He, Y. Xu, J. Zhang, and Y. Wang, Nature Materials, **1** (2020).
 - ¹³ B. Chen, F. Fei, D. Zhang, B. Zhang, W. Liu, S. Zhang, P. Wang, B. Wei, Y. Zhang, Z. Zuo, *et al.*, Nature communications **10**, 1 (2019).
 - ¹⁴ R. C. Vidal, H. Bentmann, T. R. F. Peixoto, A. Zeugner, S. Moser, C.-H. Min, S. Schatz, K. Kißner, M. Ünzelmann, C. I. Fornari, H. B. Vasili, M. Valvidares, K. Sakamoto, D. Mondal, J. Fujii, I. Vobornik, S. Jung, C. Cacho, T. K. Kim, R. J. Koch, C. Jozwiak, A. Bostwick, J. D. Denlinger, E. Rotenberg, J. Buck, M. Hoesch, F. Diekmann, S. Rohlf, M. Källäne, K. Rossnagel, M. M. Otrokov, E. V. Chulkov, M. Ruck, A. Isaeva, and F. Reinert, Phys. Rev. B **100**, 121104 (2019).
 - ¹⁵ P. Swatek, Y. Wu, L.-L. Wang, K. Lee, B. Schrunck, J. Yan, and A. Kaminski, “Gapless dirac surface states in the antiferromagnetic topological insulator mnbi_2te_4 ,” (2019), arXiv:1907.09596 [cond-mat.mtrl-sci].
 - ¹⁶ H. Li, S.-Y. Gao, S.-F. Duan, Y.-F. Xu, K.-J. Zhu, S.-J. Tian, J.-C. Gao, W.-H. Fan, Z.-C. Rao, J.-R. Huang, J.-J. Li, D.-Y. Yan, Z.-T. Liu, W.-L. Liu, Y.-B. Huang, Y.-L. Li, Y. Liu, G.-B. Zhang, P. Zhang, T. Kondo, S. Shin, H.-C. Lei, Y.-G. Shi, W.-T. Zhang, H.-M. Weng, T. Qian, and H. Ding, Phys. Rev. X **9**, 041039 (2019).
 - ¹⁷ Y.-J. Hao, P. Liu, Y. Feng, X.-M. Ma, E. F. Schwier, M. Arita, S. Kumar, C. Hu, R. Lu, M. Zeng, Y. Wang, Z. Hao, H.-Y. Sun, K. Zhang, J. Mei, N. Ni, L. Wu, K. Shimada, C. Chen, Q. Liu, and C. Liu, Phys. Rev. X **9**, 041038 (2019).
 - ¹⁸ Y. J. Chen, L. X. Xu, J. H. Li, Y. W. Li, H. Y. Wang, C. F. Zhang, H. Li, Y. Wu, A. J. Liang, C. Chen, S. W. Jung, C. Cacho, Y. H. Mao, S. Liu, M. X. Wang, Y. F. Guo, Y. Xu, Z. K. Liu, L. X. Yang, and Y. L. Chen, Phys. Rev. X **9**, 041040 (2019).
 - ¹⁹ S. H. Lee, Y. Zhu, Y. Wang, L. Miao, T. Pillsbury, H. Yi, S. Kempinger, J. Hu, C. A. Heikes, P. Quarterman, W. Ratcliff, J. A. Borchers, H. Zhang, X. Ke, D. Graf, N. Alem, C.-Z. Chang, N. Samarth, and Z. Mao, Phys. Rev. Research **1**, 012011 (2019).
 - ²⁰ D. Xiao, J. Jiang, J.-H. Shin, W. Wang, F. Wang, Y.-F. Zhao, C. Liu, W. Wu, M. H. Chan, N. Samarth, *et al.*, Physical review letters **120**, 056801 (2018).
 - ²¹ J. Li, Y. Li, S. Du, Z. Wang, B.-L. Gu, S.-C. Zhang, K. He, W. Duan, and Y. Xu, Science Advances **5**, eaaw5685 (2019).
 - ²² Y. Gong, J. Guo, J. Li, K. Zhu, M. Liao, X. Liu, Q. Zhang, L. Gu, L. Tang, X. Feng, *et al.*, Chinese Physics Letters **36**, 076801 (2019).
 - ²³ E. D. L. Rienks, S. Wimmer, J. Sánchez-Barriga, O. Caha, P. S. Mandal, J. Ruzicka, A. Ney, H. Steiner, V. V. Volobuev, H. Groiss, M. Albu, G. Kothleitner, J. Michalicka, S. A. Khan, J. Minár, H. Ebert, G. Bauer, F. Freyse, A. Varykhalov, O. Rader, and G. Springholz, Nature **576**, 423 (2019).
 - ²⁴ S. Chowdhury, K. F. Garrity, and F. Tavazza, npj Computational Materials **5**, 33 (2019).
 - ²⁵ D. Zhang, M. Shi, T. Zhu, D. Xing, H. Zhang, and J. Wang, Physical review letters **122**, 206401 (2019).
 - ²⁶ M. M. Otrokov, I. I. Klimovskikh, H. Bentmann, D. Esyunin, A. Zeugner, Z. S. Aliev, S. Gaß, A. U. B. Wolter, A. V. Koroleva, A. M. Shikin, M. Blanco-Rey, M. Hoffmann, I. P. Rusinov, A. Y. Vyazovskaya, S. V. Eremeev, Y. M. Koroteev, V. M. Kuznetsov, F. Freyse, J. Sánchez-Barriga, I. R. Amiraslanov, M. B. Babanly, N. T. Mamedov, N. A. Abdullayev, V. N. Zverev, A. Alfonso, V. Kataev, B. Büchner, E. F. Schwier, S. Kumar, A. Kimura, L. Petaccia, G. Di Santo, R. C. Vidal, S. Schatz, K. Kißner, M. Ünzelmann, C. H. Min, S. Moser, T. R. F. Peixoto, F. Reinert, A. Ernst, P. M. Echenique, A. Isaeva, and E. V. Chulkov, Nature **576**, 416 (2019).
 - ²⁷ S. V. Eremeev, M. M. Otrokov, and E. V. Chulkov, Nano letters **18**, 6521 (2018).
 - ²⁸ M. Otrokov, T. V. Menshchikova, I. Rusinov, M. Vergniory, V. M. Kuznetsov, and E. V. Chulkov, JETP Letters **105**, 297 (2017).
 - ²⁹ M. M. Otrokov, T. V. Menshchikova, M. G. Vergniory, I. P. Rusinov, A. Y. Vyazovskaya, Y. M. Koroteev, G. Bihlmayer, A. Ernst, P. M. Echenique, A. Arnau, *et al.*, 2D Materials **4**, 025082 (2017).
 - ³⁰ R. S. Mong, A. M. Essin, and J. E. Moore, Physical Review B **81**, 245209 (2010).
 - ³¹ R. Li, J. Wang, X.-L. Qi, and S.-C. Zhang, Nature Physics **6**, 284 (2010).
 - ³² J. Wang, B. Lian, and S.-C. Zhang, Physical Review B **93**, 045115 (2016).
 - ³³ A. M. Essin, J. E. Moore, and D. Vanderbilt, Physical review letters **102**, 146805 (2009).
 - ³⁴ R. C. Vidal, A. Zeugner, J. I. Facio, R. Ray, M. H. Haghighi, A. U. Wolter, L. T. C. Bohorquez, F. Caglieris, S. Moser, T. Figgemeier, *et al.*, Physical Review X **9**, 041065 (2019).
 - ³⁵ A. Zeugner, F. Nietschke, A. U. Wolter, S. Gaß, R. C. Vidal, T. R. Peixoto, D. Pohl, C. Damm, A. Lubk, R. Hentrich, *et al.*, Chemistry of Materials **31**, 2795 (2019).
 - ³⁶ P. Hohenberg and W. Kohn, Phys. Rev. **136**, B864 (1964).
 - ³⁷ W. Kohn and L. Sham, Phys. Rev. **140**, A1133 (1965).
 - ³⁸ P. Giannozzi and *et al.*, J. Phys.:Condens. Matter **21**, 395502 (2009).
 - ³⁹ J. P. Perdew, A. Ruzsinszky, G. I. Csonka, O. A. Vydrov, G. E. Scuseria, L. A. Constantin, X. Zhou, and K. Burke, Phys. Rev. Lett. **100**, 136406 (2008).
 - ⁴⁰ V. I. Anisimov, J. Zaanen, and O. K. Andersen, Phys. Rev. B **44**, 943 (1991).
 - ⁴¹ S. L. Dudarev, G. A. Botton, S. Y. Savrasov, C. J. Humphreys, and A. P. Sutton, Phys. Rev. B **57**, 1505 (1998).
 - ⁴² V. Stevanović, S. Lany, X. Zhang, and A. Zunger, Phys. Rev. B **85**, 115104 (2012).
 - ⁴³ D. R. Hamann, Phys. Rev. B **88**, 085117 (2013).
 - ⁴⁴ M. Schlipf and F. Gygi, Computer Physics Communications **196**, 36 (2015).
 - ⁴⁵ P. Scherpelz, M. Govoni, I. Hamada, and G. Galli, Journal of Chemical Theory and Computation **12**, 3523 (2016), PMID: 27331614, <https://doi.org/10.1021/acs.jctc.6b00114>.
 - ⁴⁶ A. A. Mostofi, J. R. Yates, Y.-S. Lee, I. Souza, D. Vanderbilt, and N. Marzari, Comput. Phys. Commun. **178**, 685 (2008).
 - ⁴⁷ A. A. Mostofi, J. R. Yates, Y.-S. Lee, I. Souza, D. Vanderbilt, and N. Marzari, Comput. Phys. Commun. **178**, 685 (2008).
 - ⁴⁸ N. Marzari and D. Vanderbilt, Phys. Rev. B **56**, 12847

- (1997).
- ⁴⁹ I. Souza, N. Marzari, and D. Vanderbilt, Phys. Rev. B **65**, 035109 (2001).
- ⁵⁰ Q. Wu, S. Zhang, H.-F. Song, M. Troyer, and A. A. Soluyanov, Computer Physics Communications **224**, 405 (2018).
- ⁵¹ K. F. Garrity, Phys. Rev. B **99**, 174108 (2019).
- ⁵² J. H. Lloyd-Williams and B. Monserrat, Phys. Rev. B **92**, 184301 (2015).
- ⁵³ J. Liu and D. Vanderbilt, Physical Review B **88**, 224202 (2013).
- ⁵⁴ W. Ku, T. Berlijn, C.-C. Lee, *et al.*, Physical review letters **104**, 216401 (2010).
- ⁵⁵ T. Berlijn, D. Volja, W. Ku, *et al.*, Physical review letters **106**, 077005 (2011).
- ⁵⁶ V. Popescu and A. Zunger, Physical review letters **104**, 236403 (2010).
- ⁵⁷ W. K. Hastings, Biometrika **57**, 97 (1970).
- ⁵⁸ D. Frenkel and B. Smit, in *Understanding Molecular Simulation (Second Edition)*, edited by D. Frenkel and B. Smit (Academic Press, San Diego, 2002) second edition ed., pp. 1 – 6.
-

Supplemental Materials: Topological surfaces states of MnBi_2Te_4 at finite temperatures and at domain walls

Supplementary materials. Additional details on I. tight-binding model evaluation II. the magnetic model III. the temperature dependent band structure and topology.

I. TIGHT-BINDING MODEL EVALUATION

Fig. S1 shows several more bulk comparisons of direct DFT-Wannier band structures with model band structures. Compare left and right panels.

Fig. S2a-b shows a comparison of a direct DFT calculation of a 3 septuple layer surface, including relaxations, in the layered AFM phase, with the model. While not quite as good as the bulk comparisons, the agreement is excellent.

II. MAGNETIC MODEL

We use a Heisenberg model with onsite anisotropy plus Monte Carlo sampling to generate magnetic configurations.

$$H = \frac{1}{2} \sum_{ij} J_{ij} \vec{S}_i \cdot \vec{S}_j + \sum_i A |S_i^z|^2 \quad (\text{S1})$$

We perform sampling in a $12 \times 12 \times 12$ unit cell for bulk analysis of the model. To generate spin configurations for the tight-binding model, we use a $3 \times 3 \times 5$ unit cell with the model truncated along the z direction to simulate a surface. In Fig. S3, we show the magnetic phase diagram under varying magnetic field at fixed temperature (top) and at varying temperature and zero field (bottom). We consider the ground state AFM z -direction spin configuration (blue), spins polarized FM along the z -direction (red), and spins oriented AFM between layers, but in-plane (green). We can observe a spin-flop transition in the top panel under increasing field, followed by saturation at high field.

In Fig. S4, we show the nearest neighbor in-plane (blue) and out-of-plane (red) correlation as a function of temperature. Solid lines show $\langle \vec{S}_i \cdot \vec{S}_j \rangle - \langle \vec{S}_i \rangle \cdot \langle \vec{S}_j \rangle$, which goes to zero at low temperature, while dashed lines show $\langle \vec{S}_i \cdot \vec{S}_j \rangle$, which goes to one below the phase transition. In-plane correlations are much larger and remain significant to higher temperatures, which is consistent with the shorter distances between Mn atoms in-plane and the much larger magnetic interaction coefficients (J_{ij}) in-plane.

III. TEMPERATURE DEPENDENT TOPOLOGY AND BAND STRUCTURES

Fig. S5 (bottom) shows the average Chern number for the $3 \times 3 \times 5$ with surfaces system studied in Fig. 2 in the main text, as a function of temperature. While for any single magnetic snapshot, the Chern number is always an integer, the average over many snapshots can indicate how robust the topology is relative to magnetic fluctuations. We expect that in a very large unit cell, instead of the snapshots of a small periodic cell that we can calculate, the Chern number would not fluctuate, but the local electronic structure and local band gap would fluctuate and approach zero in regions close to but below the Néel temperature.

In Fig. S6, we show bulk versions of the band structures in Fig. 2 in the main text, in $3 \times 3 \times 6$ unit cells unfolded to $1 \times 1 \times 6$ cells. Note the lack of states in the gap, and the relatively small changes in electronic structure besides averaging of spin-polarized bands above T_N .

* kevin.garrity@nist.gov

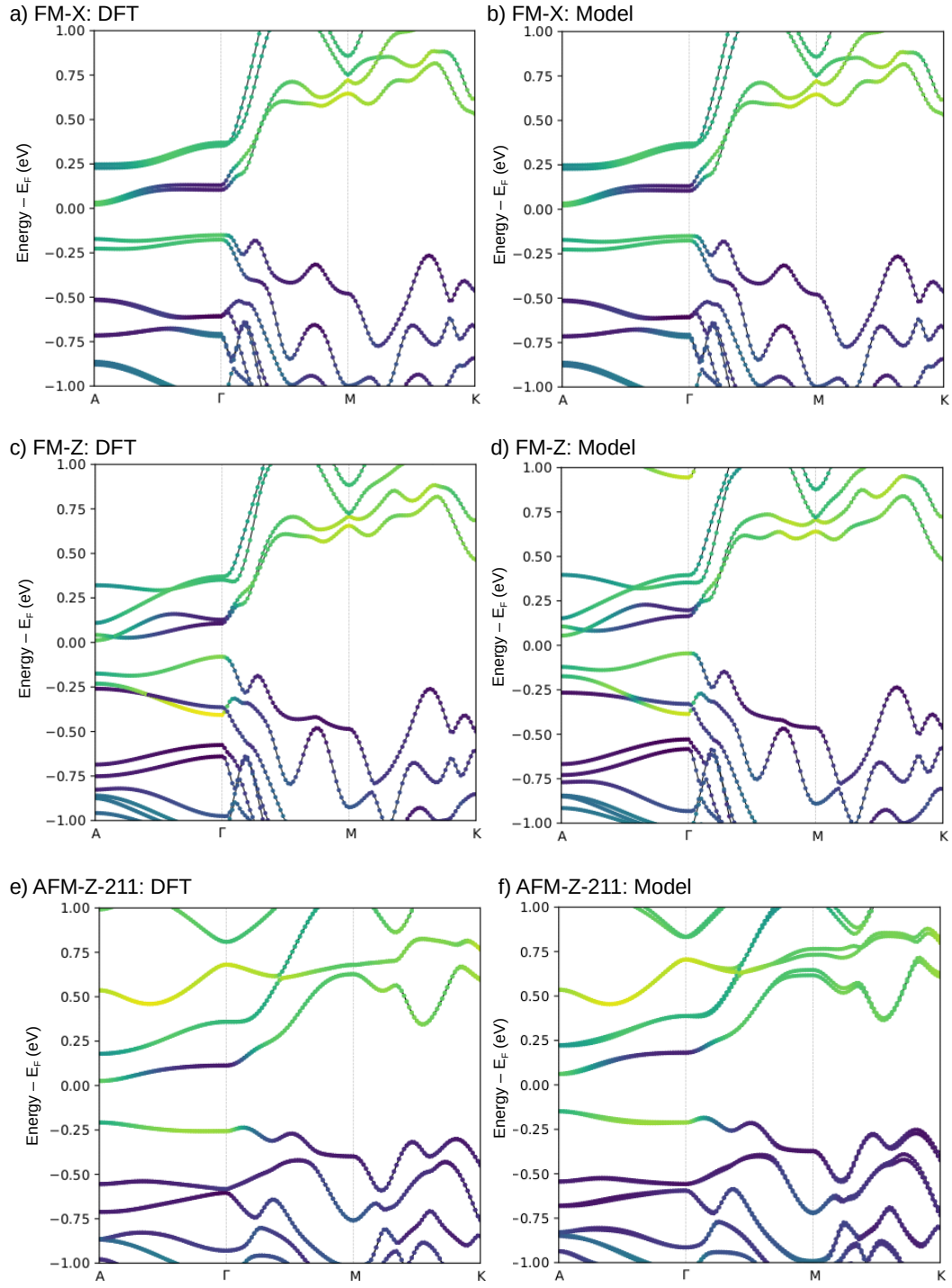


FIG. S1. Comparison of DFT and model band structures, as in Fig. 1. a,c,e) DFT, b,c,d) Model. a-b) FM, spins in x -direction. c-d) FM, spins in z -direction, e-f) AFM, spins in $\pm z$ direction, alternating in-plane (not the ground state).

a) DFT 3 layer slab w/surfaces, AFM

b) Model, same

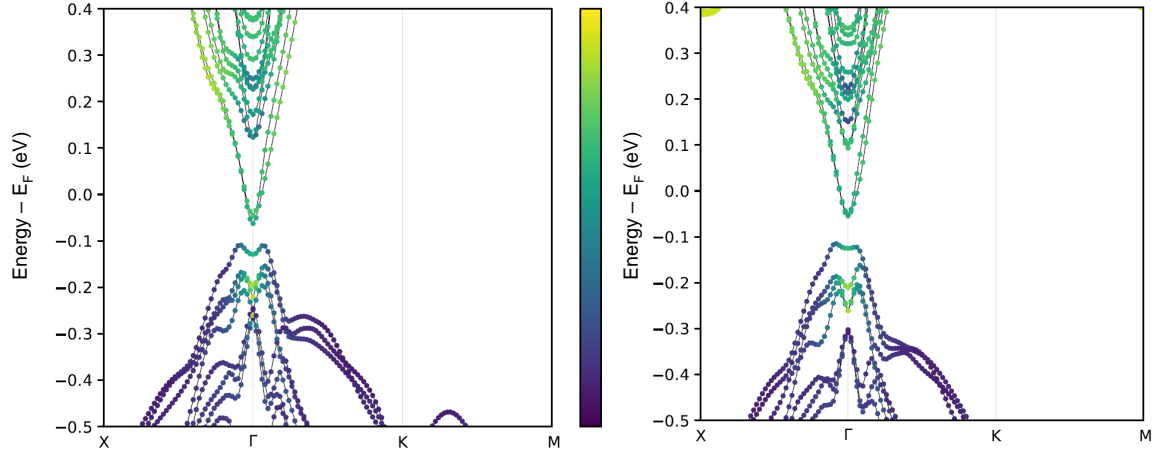


FIG. S2. Comparison of DFT and model band structures, 3 layer slab with surfaces, with AFM spin ordering, spins in $\pm z$ -direction. a) DFT, b) Model. DFT includes surface relaxations.

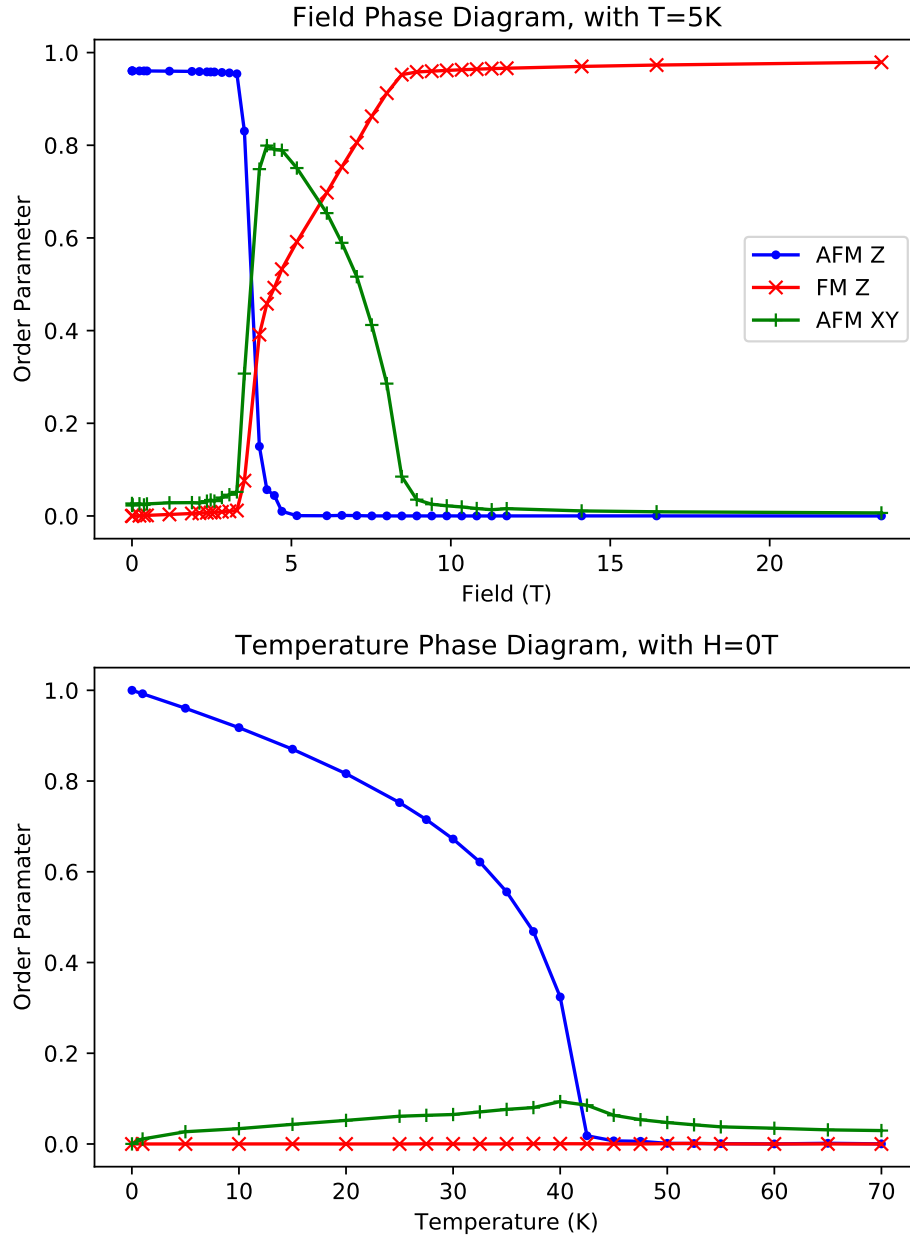


FIG. S3. Magnetic phase diagram as a function of field (top) and temperature (bottom). See text. Error bars are smaller than symbols.

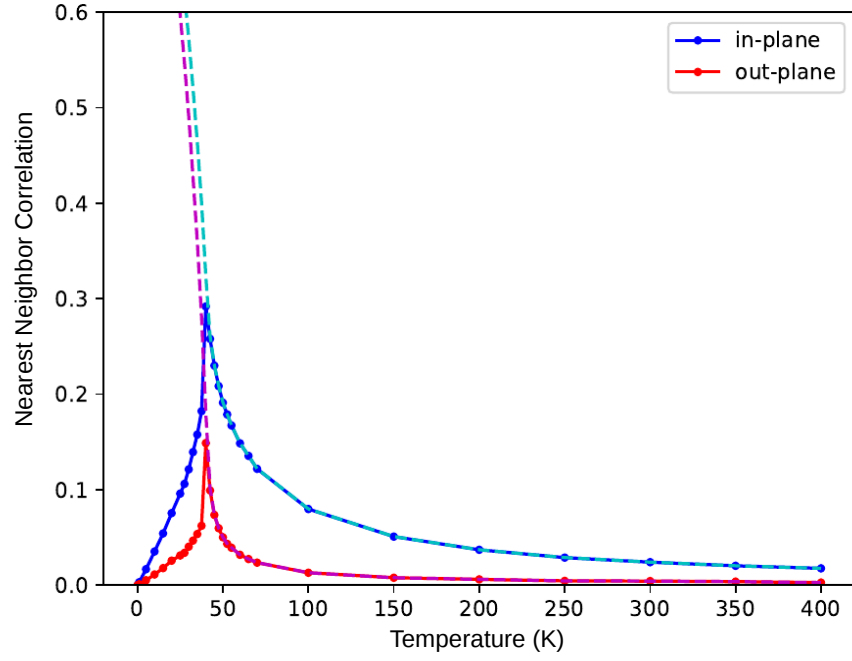


FIG. S4. Magnetic nearest neighbor spin-spin correlation as a function of temperature at zero field. Blue line is in-plane correlation, red line is out-of-plane correlation. See text.

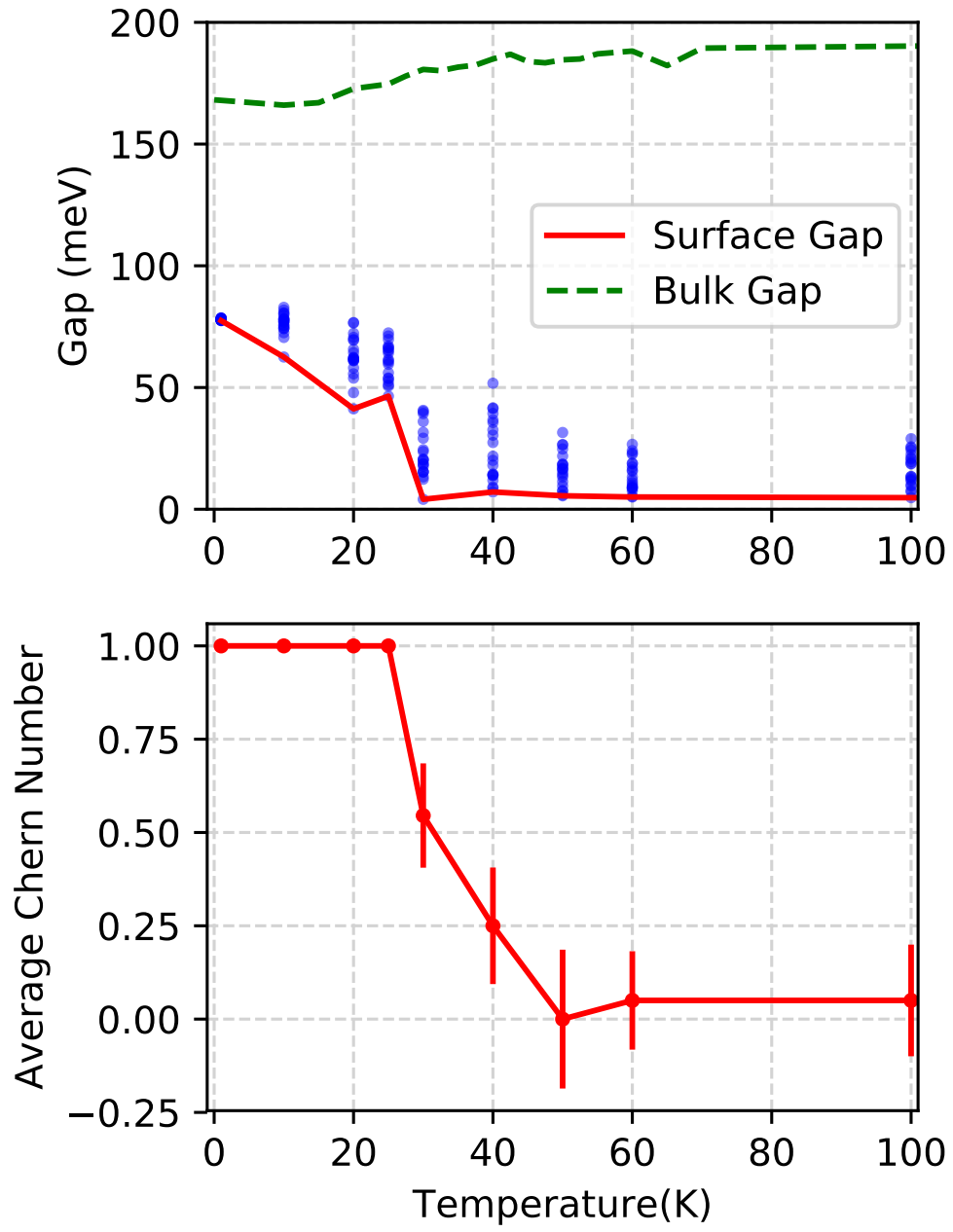


FIG. S5. Top: same as Fig. 2a. Bottom: Average Chern number as function of temperature. Error bars show 1 standard deviation statistical error.

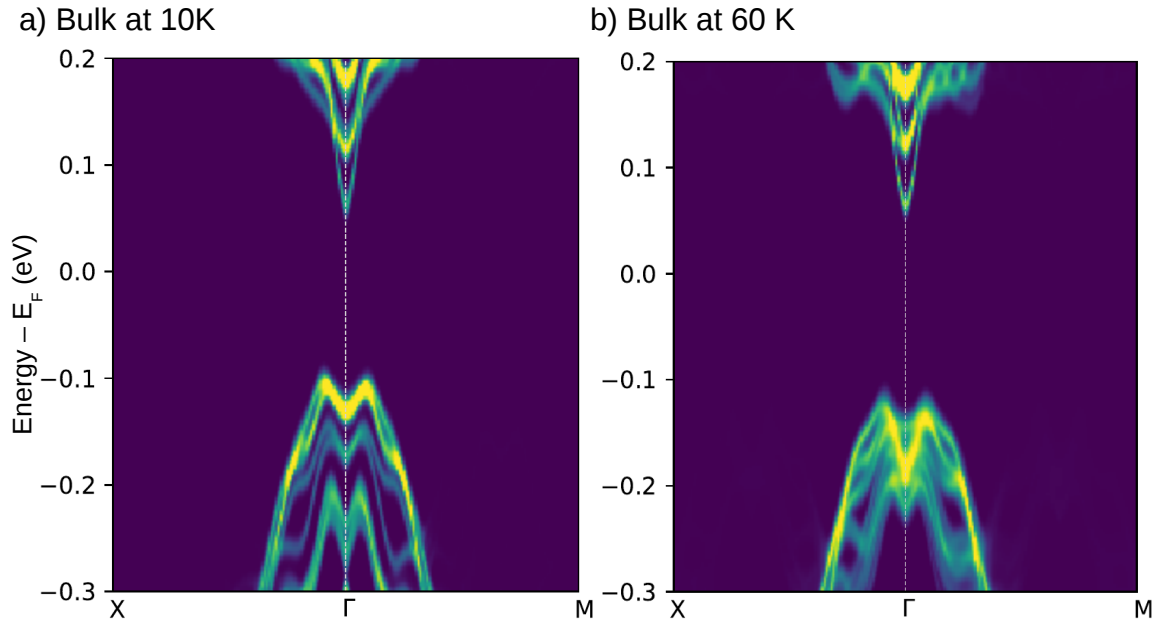


FIG. S6. Bulk band structure in $3 \times 3 \times 6$ unit cell, periodic in all three directions (no surface), unfolded to $1 \times 1 \times 6$ unit cell, for comparison with Fig. 2 b-d. a) 10 K b) 60 K.